ARTICLE IN PRESS

Physics of the Earth and Planetary Interiors xxx (2011) xxx–xxx

Contents lists available at SciVerse ScienceDirect

Physics of the Earth and Planetary Interiors

journal homepage: www.elsevier.com/locate/pepi

Numerical and experimental investigation of shear-driven inertial oscillations in an Earth-like geometry

H. Matsui [a], M. Adams [b], D. Kelley [b,c], S.A. Triana [b], D. Zimmerman [b], B.A. Buffett [a,*], D.P. Lathrop [b]

[a] Department of Earth & Planetary Science, University of California, Berkeley, CA 94720, United States
[b] Department of Physics, University of Maryland, College Park, MD 20742, United States
[c] Department of Mechanical Engineering & Material Science, Yale University, New Haven, CT 06520, United States

ARTICLE INFO

Article history:
Received 17 December 2010
Received in revised form 19 July 2011
Accepted 28 July 2011
Available online xxxx
Edited by: Keke Zhang.

Keywords:
Earth's core
Inertial waves
Magnetic fields

ABSTRACT

Inertial waves and small-scale turbulence are inevitable consequences of rapid rotation and low viscosity in the Earth's core. We use numerical simulations and experiments to investigate the influence of waves and turbulence on the large-scale flow of an electrically conducting fluid in a spherical annulus. The large-scale flow is driven by shear between the inner-core and outer-core boundaries in the presence of a vertical magnetic field. The rotation rates of the inner and outer boundaries are denoted by Ω_i and Ω_o, respectively, which define a Rossby number $Ro = (\Omega_i - \Omega_o)/\Omega_o$. We focus on small negative values ($-1 < Ro < 0$), where inertial modes have been previously reported in the experiments. Inertial modes are also identified in the simulations at sufficiently low Ekman number. Good agreement with the experiments is obtained for both the spatial structure and frequency of the inertial modes. The experimental results provide an important benchmark for the simulations, while the simulations provide detailed information about the flow, assisting in the interpretation of the experiments. We find that the magnetic field suppresses small-scale flow that would otherwise be present if the sole source of dissipation was due to fluid viscosity.

© 2011 Elsevier B.V. All rights reserved.

1. Introduction

Experiments in fluid dynamics have long contributed to our understanding of the Earth's interior. Laboratory models are capable of producing complex, turbulent flows that are well beyond the reach of current numerical simulations (e.g., Sumita and Olson, 2003; Schmitt et al., 2008; Monchaux et al., 2007). Insights from experiments provide both qualitative descriptions of physical processes and quantitative estimates of specific properties of the flow. Laboratory models can also be used to test numerical simulations where other means of verification are not available. In the present study we use laboratory models of the spherical Couette flow (Kelley et al., 2007) to test a numerical simulation of rapidly rotating flow. The numerical simulation is limited in the choice of experimental conditions by the need to resolve the flow at the smallest scales. However, a wider range of experimental conditions can be explored using large-eddy simulations (LES), provided suitable models are available for the effects of subgrid-scale turbulence (Matsushima, 2005; Matsui and Buffett, 2005, 2007; Chen and Jones, 2008). We present the results of a resolved numerical simulation of the spherical Couette flow, which successfully reproduces observations from the experiments. We also obtain good numerical results using a LES on a coarser grid, although the subgrid-scale model does not appear to dissipate enough kinetic energy at small scales. By combining experiments and simulations we gain insight into the role of small-scale turbulence and improve the subgrid-scale models.

Both the experiments and the numerical simulations reveal a broad range of temporal fluctuations in the flow. Discrete periodicities due to inertial oscillations are superimposed on a mean background flow and random fluctuations. Inertial oscillations in the experiments are primarily antisymmetric about the equator, based on measurements of the external magnetic field induced by interactions between the waves and an imposed (vertical) magnetic field. This interpretation is confirmed using the numerical simulations. The inertial waves are thought to be generated by fluctuations in the mean flow and selectively amplified by reflections from shear layers in the fluid through a process known as over-reflection (Ribner, 1957). Kelley and Lathrop (2010) show that the selection of inertial waves by over-reflection provides a good description of the experimental results; interaction between shear layers and boundary layer eruptions may provide an alternate explanation (Rieutord and Valdettaro, 2010). Differences in the damping of the inertial oscillations may also play a role in wave selection. The numerical simulations presented here reproduce the selection of inertial waves in the spherical Couette flow and provide additional insights into the underlying dynamics. In

* Corresponding author.
E-mail address: bbuffett@berkeley.edu (B.A. Buffett).

0031-9201/$ - see front matter © 2011 Elsevier B.V. All rights reserved.
doi:10.1016/j.pepi.2011.07.012

particular, the simulations reveal the structure of zonal flow and indicate that inertial oscillations are largely confined to the region outside the tangent cylinder.

We begin with a brief discussion of the experimental setup and the identification of inertial oscillations using measurements of magnetic field perturbations outside the fluid shell. The numerical model is adapted from the finite-element dynamo model of Matsui and Okuda (2005). Numerical results for the frequency and spatial structure of the external magnetic field are compared with the results of the experiments to assess the validity of the numerical solution. The LES model provides similar results for the frequency and spatial structure of the external magnetic field, although there are differences in the kinetic energy spectra between the resolved and LES solutions. We attribute the difference to the SGS model; it appears that SGS model fails to dissipate enough kinetic energy at the smallest scales.

2. Experimental setup

Our experimental device, sketched in Fig. 1, is a spherical Couette cell with independently rotating inner and outer spheres, as described previously (Kelley et al., 2007; Kelley and Lathrop, 2010). The outer, titanium sphere has inner radius $r_o = 30.5$ cm, wall thickness 2.54 cm, and magnetic diffusivity 0.044 $m^2\,s^{-1}$. The inner, solid copper sphere has radius $r_i = 10$ cm and magnetic diffusivity 0.014 $m^2\,s^{-1}$. The gap between them is filled with about 110 L of liquid sodium, kept between 100 and 110 °C by an array of 20 incandescent heaters, each 0.5 kW, mounted near the lower hemisphere of the experiment. Each sphere is coupled to an AC induction motor controlled by a variable frequency drive, so that the rotation rates and directions of the spheres can be controlled independently. We have previously rotated the inner sphere as fast as $|\Omega_i| = 283\ s^{-1}$ and the outer sphere as fast as $|\Omega_o| = 220\ s^{-1}$; the data discussed below were recorded with the outer sphere rotating at 113 s^{-1} and the inner sphere rotating at 45.2 s^{-1}. The inner sphere is supported by a 25 mm stainless steel shaft that rotates at Ω_i. That shaft, in turn, is supported by bearings housed in cylindrical chambers, 8.89 cm in diameter, that extend from the outer sphere and rotate at Ω_o. The necessity of support shafts in a laboratory device causes the shape of our apparatus to deviate slightly from the true spherical Couette geometry used in the simulations described below. Nonetheless we find that many behaviors match closely, as will be described.

We apply a steady magnetic field $B_0 = 12$ mT parallel to the rotation axis using a pair of external electromagnets. The sodium test fluid is an excellent electrical conductor, with magnetic diffusivity 0.084 $m^2\,s^{-1}$, which allows for electromagnetic induction by the fluid motion in the presence of the applied field B_0. We characterize the flow by measuring that induction with an array of 30 Hall probes (Honeywell SS94A1F) mounted around the fluid cell. Each probe records the local cylindrical radial component of the magnetic field (horizontal and toward the axis of rotation) as a function of time, sampled 1024 times per second. This rate is substantially faster than the flow timescales, even after translation from the rotating frame to the laboratory frame. The probes are mounted at distances $35.6 \leqslant r \leqslant 40.6$ cm from the center of the sphere ($1.16 r_o \leqslant r \leqslant 1.33 r_o$) in an arrangement chosen to be well-suited for projection onto the vector spherical harmonics, yielding Gauss coefficients up to degree and order four. We perform that projection using a standard linear least-squares calculation. The accuracy of the calculation is optimized by making measurements at locations where the vector spherical harmonic modes are most readily distinguished from each other. To state the same fact in mathematical terms, the accuracy of the least-squares fit depends on the condition number of the matrix of the normal equations (Press et al., 2007), based on the three-dimensional location of each probe. The array used here, closely following a previous design (Sisan, 2004), yields a condition number $C = 22$, superior to any of more than 10^6 alternate arrangements constructed in a Monte Carlo analysis. Below we show spatially resolved magnetic fields using measurements made with this probe array. We also show time histories of the induced field, based on a single (more sensitive) probe mounted on the equator (Ohio Semitronics HR72).

3. Numerical model

We simulate the flow of an electrically conducting fluid in a spherical shell using the dynamo model of Matsui and Okuda (2005). Buoyancy forces are replaced with mechanical forcing due to differential rotation between the inner and outer boundaries. Both the inner sphere and the solid outer shell have finite electrical conductivity, which permits magnetic shear stresses at the boundaries of the fluid. For simplicity we use the same conductivity for the solid inner sphere, fluid region and solid outer shell that contains the fluid. The region outside the solid outer shell is assumed to be an insulator. A potential field is calculated in the insulating region on a grid that extends to a radius r_m, which is 17× larger than the outer radius of the fluid shell (denoted by r_o).

A total of 48 radial levels are used in the fluid with finer resolution near the boundaries to resolve thin viscous boundary layers (see Fig. 2). The mesh is based on a cubed sphere with a total of

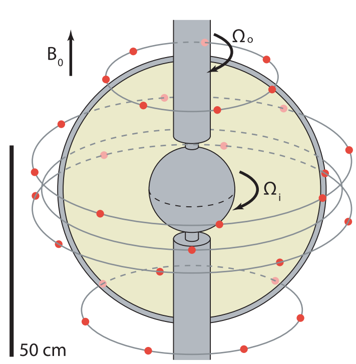

Fig. 1. Schematic illustration of the spherical Couette experiment. Fluid motion is driven by differential rotation between the inner and outer boundaries of the fluid shell. A vertical magnetic field $\mathbf{B}_0$ is imposed and magnetic perturbations are recorded by an array of Hall probes, each oriented along the direction of a cylindrical radius.

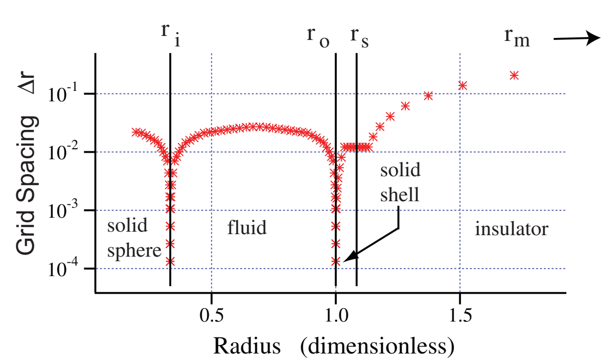

Fig. 2. Narrow grid spacing in spherical radius, Δr, is used near the fluid boundaries, $r = r_i$ and $r = r_o$, to resolve the viscous boundary layer. A courser grid is used in the insulating region to describe the potential field. The insulating region extends from $r = r_s$ to $r = r_m$. The outer radius of the solid shell is $r_s = 1.08 r_o$ and the outer radius of the insulating region is $r_m = 17 \times r_o$.

Please cite this article in press as: Matsui, H., et al. Numerical and experimental investigation of shear-driven inertial oscillations in an Earth-like geometry. Phys. Earth Planet. In. (2011), doi:10.1016/j.pepi.2011.07.012

340,000 nodes; there are 96 nodes distributed around the equator, yielding an average horizontal resolution of 0.01 m. A constant time step of 6×10^{-5} s is used in all calculations and a typical run has 2×10^5 time steps, corresponding to an integration time of 12 s or about 60 revolutions. The initial condition is taken from a prior simulation in which the fluid is spun up in the absence of an imposed magnetic field.

The Navier–Stokes equation for the fluid velocity $\mathbf{u}$ is expressed in a reference frame that rotates with the angular velocity of the outer shell $\Omega_o\hat{\mathbf{z}}$. We adopt r_o as a length scale, Ω_o^{-1} as a timescale and use the amplitude of the imposed magnetic field $\mathbf{B}_0 = B_0\hat{\mathbf{z}}$ as the scale for the magnetic field. The non-dimensional equations for the fluid velocity are

$$\frac{\partial \mathbf{u}}{\partial t} + \mathbf{u}\cdot\nabla\mathbf{u} + 2\hat{\mathbf{z}}\times\mathbf{u} = -\nabla P + E\nabla^2\mathbf{u} + \Lambda(\nabla\times\mathbf{b})\times(\hat{\mathbf{z}}+\mathbf{b}) \qquad (1)$$

and

$$\nabla\cdot\mathbf{u} = 0 \qquad (2)$$

where P is the modified pressure (including centrifugal forces) and $\mathbf{b}$ is the magnetic perturbation due to fluid motion. Two dimensionless parameters appear in Eq. (1); one is the Ekman number, $E = \nu/\Omega_o r_o^2$ and the other is a modified Elsasser number, $\Lambda = u_a^2/u_o^2$, where $u_o = \Omega_o r_o$ is the velocity scale and $U_a = B_0/\sqrt{\rho\mu}$ is the speed of Alfven waves. Here ρ is the fluid density and μ is the magnetic permeability.

The magnetic perturbation is expressed in terms of a vector potential $\mathbf{A}$ to more easily accommodate continuity conditions at jumps in electrical conductivity (see below). The vector potential is defined by

$$\mathbf{b} = \nabla\times\mathbf{A} \qquad (3)$$

and obeys

$$\frac{\partial \mathbf{A}}{\partial t} = -\nabla\phi + (\mathbf{u}\times\mathbf{b}) + Rm^{-1}\nabla^2\mathbf{A} \qquad (4)$$

and

$$\nabla\cdot\mathbf{A} = 0 \qquad (5)$$

where $Rm = u_o r_o/\eta$ is the magnetic Reynolds number and ϕ is a scalar electric potential that enforces the Coulomb gauge in (5). The physical properties and dimensionless parameters for the experiments and numerical simulations are listed in Table 1.

We note two differences between the experimental and simulation conditions. First, the rotation rate of the outer and inner spheres is slower in the simulation, although the relative rotation is the same. A higher rotation in the experiments yields a low Ekman number ($E = 7 \times 10^{-8}$) which is too small to handle in the simulations. However, we can achieve an Ekman number of $E = 2.6 \times 10^{-7}$, ensuring that the effects of viscosity are small. Thin viscous boundary layers in the numerical simulation require very high radial resolution near the boundaries. Second, we impose a magnetic field in the simulation that is slightly larger than that in the experiments. A higher field increases the Elsasser number relative to the experiments, although the value is still small (i.e. $\Lambda \ll 1$). However the higher field causes greater ohmic losses at small length scales in the simulations and suppresses the amplitude of flow at these small scales.

No-slip boundary conditions are imposed on the velocity at the inner and outer boundaries of the fluid shell (denoted by radius r_i and r_o, respectively). The inner shell rotates with angular velocity Ω_i, so the velocity of the inner boundary in the rotating frame is

$$\mathbf{u} = \left(\frac{\Omega_i}{\Omega_o} - 1\right)\hat{\mathbf{z}}\times\mathbf{x} \equiv Ro\hat{\mathbf{z}}\times\mathbf{x} \qquad (6)$$

where $\mathbf{x}$ is the position vector and the Rossby number $Ro = \Omega_i/\Omega_o - 1$ is a non-dimensional measure of the fluid forcing. The same velocity is used inside the conducting solid sphere ($r < r_i$) to solve the induction equation in (4). The velocity vanishes at $r = r_o$ and through the solid outer shell ($r_o < r < r_s$) in the solution of the induction equation. Boundary conditions for the induction equation require continuity of the vector potential $\mathbf{A}$, the radial gradient $\partial\mathbf{A}/\partial r$ and the electric potential ϕ at the inner and outer boundaries of the fluid. At the outer radius of the insulating region (i.e. r_m), we require

$$\mathbf{A} = \frac{\partial\phi}{\partial r} = 0 \qquad (7)$$

We evaluate the potential field at $r = 1.21r_o$, based on the average location of the Hall probes in the experiment.

4. Direct numerical simulations

Fig. 3 shows a snapshot of the azimuthal component of flow on a vertical cross section through the fluid shell in the frame rotating with the outer boundary. Slower rotation of the inner sphere ($\Omega_i = 0.4\Omega_o$ or $Ro = -0.6$) drives an eastward (negative) velocity in the rotating frame. The eastward flow near the inner sphere

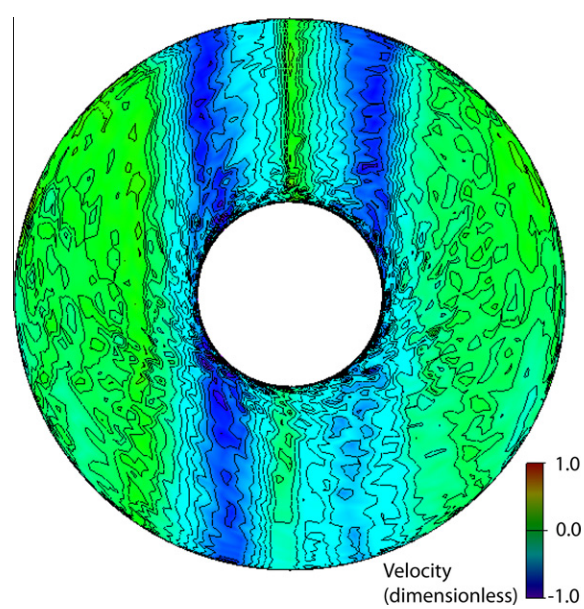

Fig. 3. A snapshot of azimuthal flow in the numerical simulation. Strong shear layers (Stewartson layers) develop at the tangent cylinder in response to differential rotation of the inner and outer boundaries. The mean flow outside the tangent cylinder is weak with small-scale fluctuations due to turbulence.

Table 1
Parameters and physical properties in experiment and numerical simulation.

Parameter	Symbol	Experiment	Simulation
Rotation rate (outer)	Ω_o	113 s^{-1}	31.4 s^{-1}
Rotation rate (inner)	Ω_i	45.2 s^{-1}	12.6 s^{-1}
Radius (outer)	r_o	0.305 m	0.305 m
Radius (inner)	r_i	0.102 m	0.102 m
Magnetic field	B_0	12 mT	14 mT
Fluid density	ρ	927 kg m^{-3}	927 kg m^{-3}
Viscosity	ν	7.4×10^{-7} m^2 s^{-1}	7.4×10^{-7} m^2 s^{-1}
Magnetic diffusivity	η	0.084 m^2 s^{-1}	0.084 m^2 s^{-1}
Radius ratio	R_i/R_o	0.33	0.33
Rotation ratio	Ω_i/Ω_o	0.40	0.40
Rossby number	Ro	−0.6	−0.6
Ekman number	E	7.0×10^{-8}	2.6×10^{-7}
Elsasser number	Λ	1.0×10^{-4}	1.8×10^{-3}
Magnetic Prandtl	Pm	8.8×10^{-6}	8.8×10^{-6}

Please cite this article in press as: Matsui, H., et al. Numerical and experimental investigation of shear-driven inertial oscillations in an Earth-like geometry. Phys. Earth Planet. In. (2011), doi:10.1016/j.pepi.2011.07.012

ARTICLE IN PRESS

extends in the direction of the rotation axis due to the effect of rapid rotation, forming a cylinder that is approximately tangent to the equator of the inner sphere. (We subsequently refer to this surface as the tangent cylinder.) The mean zonal flow inside the tangent cylinder is approximated by solid body rotation, although there are large fluctuations about the mean.

Small-scale flow is evident throughout the fluid shell. Deviations from the mean zonal flow represent about 15% of the total kinetic energy, or about 38% of the amplitude of the velocity field. The mean azimuthal flow outside the tangent cylinder is relatively weak, indicating that the fluid is nearly stationary with respect to the outer shell. A strong shear flow develops near the tangent cylinder in a region commonly called the Stewartson layer (Stewartson, 1966). The Stewartson layer is axisymmetric in the simplest case, but high shear can cause instabilities of the Stewartson layer, producing non-axisymmetric flow (Hollerbach, 2003). It is likely that these shear instabilities contribute to deviations from the mean zonal flow in the simulation.

Fig. 4 shows time-averaged spectra of kinetic and magnetic energy from the simulation as a function of angular order m. (The spectra are computed by interpolating the velocity and magnetic fields onto a spherical grid; the resulting fields are decomposed into vector spherical harmonics and the energies are determined using the orthogonality of the spherical harmonics.) The large toroidal component of velocity at $m = 0$ represents the azimuthal flow (as shown in Fig. 3), whereas the poloidal component represents a meridional circulation, probably due to Ekman pumping and flow within the Stewartson layers. The kinetic energy at $m = 1$ and 2 is large relative to the trend at higher m. The energy at $m = 1$ is consistent with predictions for shear instabilities, which draw energy from the zonal flow (Hollerbach, 2003). Large-amplitude waves at $m = 2$ (described below) probably contribute to the anomalous energy observed at this angular wavenumber.

Nonlinear interactions are responsible for transferring energy to higher m, where a combination of viscous and ohmic friction dissipates the flow.

The absence of a strong mean flow outside the tangent cylinder means that fluctuations in the flow are well described by motion in a uniformly rotating fluid. As a consequence the region outside the tangent cylinder is expected to support inertial waves. Discrete inertial modes are likely to have frequencies that are well approximated by the frequencies of inertial modes in a sphere, particularly if the wave motion is confined to the region outside the tangent cylinder. The dominant waves observed in both the experiment and the numerical simulation appear to satisfy this condition, justifying quantitative comparisons with theoretical frequencies of inertial modes in a full fluid sphere.

The motion of the electrically conducting fluid distorts the imposed vertical magnetic field, producing fluctuations inside the fluid and a time-dependent potential field outside the apparatus. Fig. 5 shows the spectrum of time variations in the B_s component of the field, measured by a single Hall probe mounted at the equator in the experiments. The dimensionless frequency ω_{lab}/Ω_o refers to the non-rotating (laboratory) frame of the Hall probes. The corresponding spectrum from the numerical simulation is shown for comparison in the lower panel of Fig. 5. A dominant frequency in both the experiments and simulations occurs at $\omega_{lab}/\Omega_o = 1.5$. Smaller peaks at $\omega_{lab}/\Omega_o = 0.6$ and 2.5 are also evident in the experiments and the simulations. A peak at $\omega_{lab}/\Omega_o = 1$ in the experiments may reflect electrical noise from the AC motors.

Insights into the origin of the frequencies in the experiments and simulations are inferred from the spatial structure of the

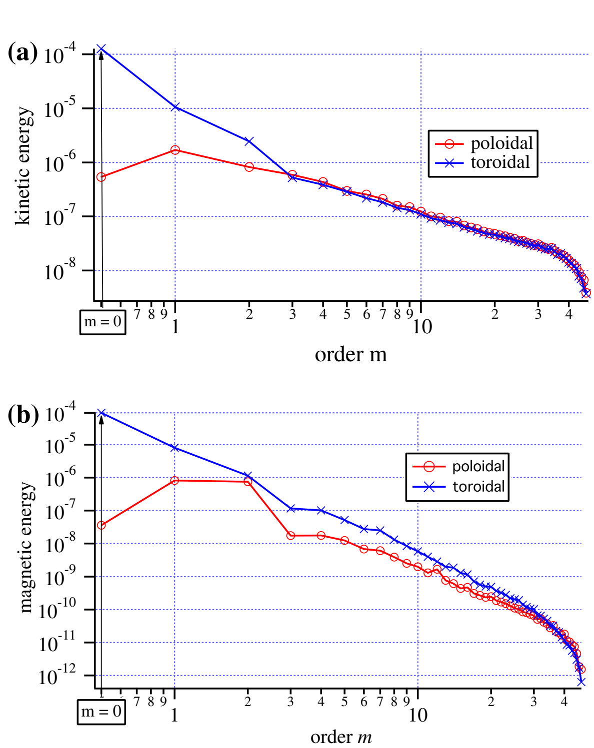

Fig. 4. Spatial spectrum of (a) kinetic energy and (b) magnetic energy as a function of angular order m. Strong zonal flow ($m = 0$) is unstable to non-zonal perturbations. The large energy at $m = 1$ is attributed to a shear instability described by Hollerbach (2003), while the energy at $m = 2$ is associated with an inertial model. A combination of ohmic and viscous losses damps the fluid motion at small scales.

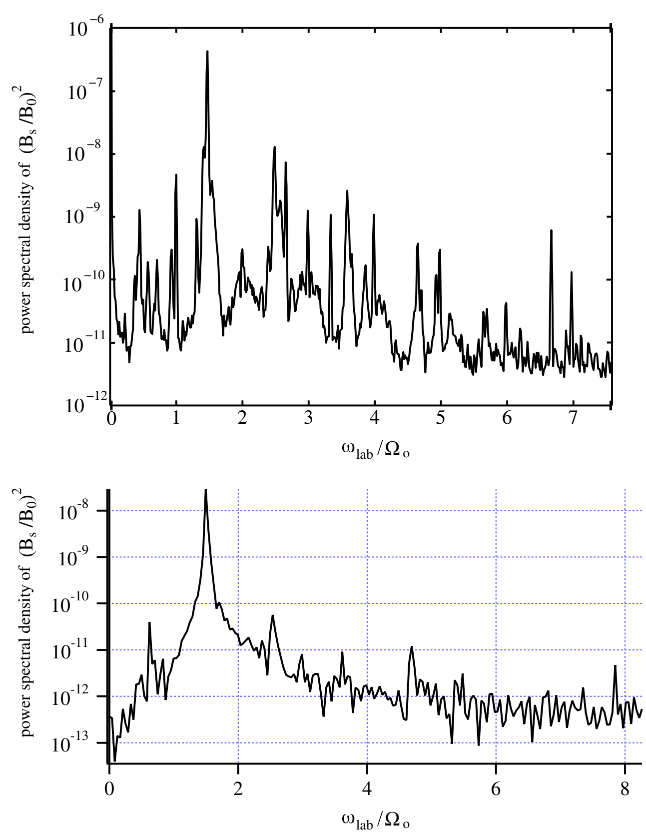

Fig. 5. Spectrum of time variations in the potential field from the experiment (top) and from the numerical simulation (bottom). The frequency ω_{lab}/Ω_o refers to the time variations in the laboratory (non-rotating) frame. Narrow peaks in the spectra are attributed to inertial oscillations, which are excited by differential rotation.

Please cite this article in press as: Matsui, H., et al. Numerical and experimental investigation of shear-driven inertial oscillations in an Earth-like geometry. Phys. Earth Planet. In. (2011), doi:10.1016/j.pepi.2011.07.012

potential field. The magnetic potential in the insulating region is represented by Gauss coefficients (g_l^m, h_l^m) in a spherical harmonic expansion (Bullard and Gellman, 1954). A single spherical harmonic with degree l and order m is denoted by $Y_l^m(\theta, \phi)$, where θ is the colatitude and ϕ is the longitude. Fig. 6 shows the temporal evolution of (g_2^2, h_2^2) and (g_4^2, h_4^2) in the rotating frame from the numerical simulation. The corresponding spectra are also shown in Fig. 6, where the frequency ω/Ω_o also refers to the rotating frame. These two sets of Gauss coefficients share a common frequency, $\omega/\Omega_o = -0.49$, where the negative sign indicates westward traveling waves in the rotating frame (i.e. opposite to the direction of rotation).

Frequencies of waves in the laboratory frame are related to frequencies in the rotating frame by

$$\frac{\omega_{lab}}{\Omega_o} = m + \frac{\omega}{\Omega_o} \quad (8)$$

where m is the azimuthal wavenumber of the spherical harmonics that characterize the waves. For the wave associated with $m = 2$ in Fig. 6 we obtain a frequency of $\omega_{lab}/\Omega_o = 1.5$, which is the dominant frequency in the experiments. A similar treatment of the other Gauss coefficients can be used to identify other spectral peaks in the experiments. For example, the Gauss coefficients (g_3^3, h_3^3) from the numerical simulation are shown in Fig. 7. These coefficients exhibit a more complicated time dependence and produce a broader spectrum around a peak at $\omega/\Omega_o = -0.46$. The corresponding frequency in the laboratory frame appears to explain the observed frequency at $\omega_{lab}/\Omega_o = 2.5$. We also find time variations in (g_3^1, h_3^1) and (g_5^1, h_5^1) in the simulation with a dominant frequency of $\omega/\Omega_o = -0.37$. This particular wave can explain the spectral peak at $\omega_{lab}/\Omega_o = 0.62$ in both the experiments and the numerical simulation. In summary, the dominant peaks in the spectrum of potential field variations are associated with specific spatial patterns. A connection between the frequencies and spatial patterns is established by the theory of inertial oscillations in a sphere. We conclude this section by showing that the experiments and simulations exhibit the same correspondence between frequency and spatial structure.

The spatial structure of the potential field in the experiments is reconstructed using measurements from the array of Hall probes (see Kelley and Lathrop (2010) for details). Fig. 8 shows the spatial structure of the B_s field, after bandpass filtering the measurements

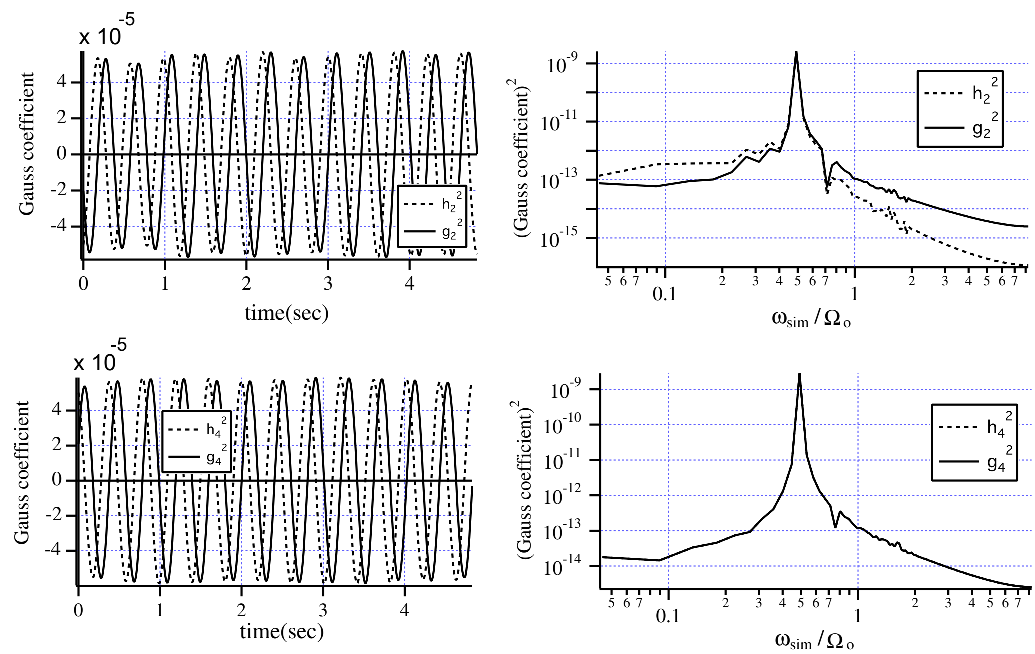

Fig. 6. Time dependence of Gauss coefficients (g_2^2, h_2^2) and (g_4^2, h_4^2) (left) and the corresponding spectra (right) from the numerical simulation in the rotating frame. A simple periodic dependence produces a strong peak in the spectrum at $\omega/\Omega_o = 0.49$.

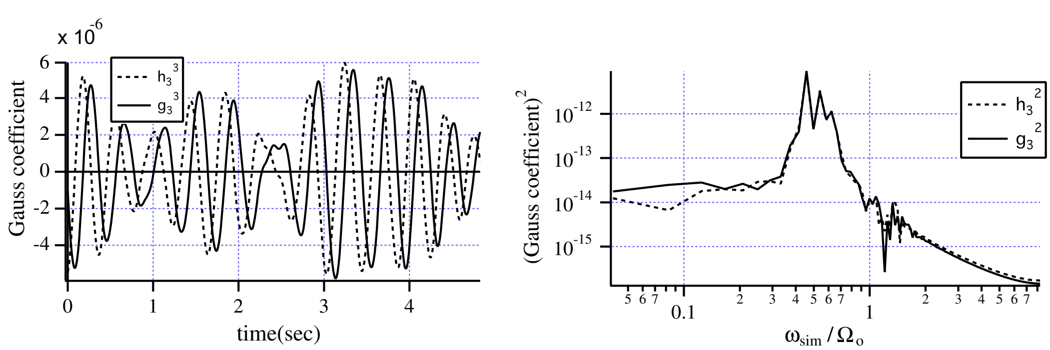

Fig. 7. Time dependence of Gauss coefficients (g_3^3, h_3^3) (left) and spectra (right) from the numerical simulation. A more complicated time dependence produces a broader spectrum with a peak at $\omega/\Omega_o = 0.46$.

Please cite this article in press as: Matsui, H., et al. Numerical and experimental investigation of shear-driven inertial oscillations in an Earth-like geometry. Phys. Earth Planet. In. (2011), doi:10.1016/j.pepi.2011.07.012

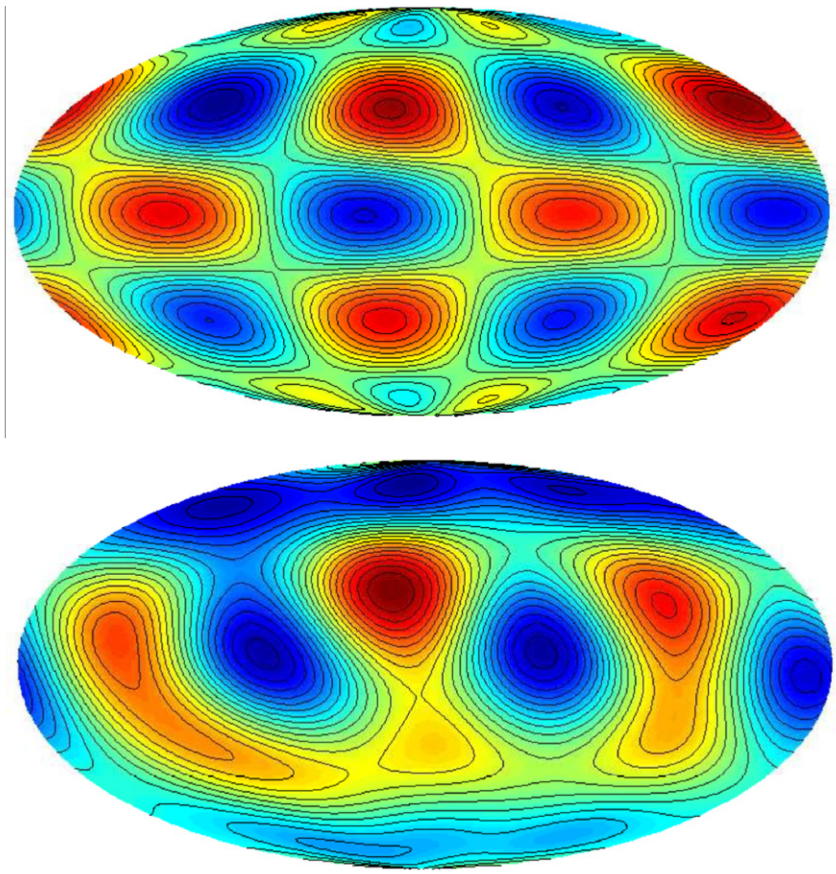

Fig. 8. Spatial pattern of the B_s component of the field constructed from the Hall probe measurements in the experiments. (Top) Applying a bandpass filter to the measurements ($1.25 < \omega_{lab}/\Omega_o < 1.75$) reveals a dominant Y_4^2 pattern. (Bottom) A bandpass filter at $2.25 < \omega_{lab}/\Omega_o < 2.75$ isolates a wave with a strong Y_3^3 component, although other spherical harmonic components are also present.

to a narrow range of frequencies around the two dominant frequencies, $\omega_{lab}/\Omega_o = 1.5$ and 2.5. The measured field at $\omega_{lab}/\Omega_o = 1.5$ represents a wave with $m = 2$. Both Y_2^2 and Y_4^2 components are present in the spatial pattern, although the Y_4^2 component is most prominent in Fig. 8. The measured field at $\omega_{lab}/\Omega_o = 2.5$ (bottom panel in Fig. 8) corresponds to a wave with $m = 3$. The principal spherical harmonic component is Y_3^3, although a simple Y_3^3 pattern cannot explain the change in sign along the meridians of longitude. This means that the observed field includes other spherical harmonic components. However, the dominant Y_3^3 pattern for the wave at $\omega_{lab}/\Omega_o = 2.5$ is consistent with the frequency of the (g_3^3, h_3^3) coefficients in the numerical simulations.

The amplitudes of coefficients (g_3^3, h_3^3) are small compared with the contributions from (g_2^2, h_2^2) and (g_4^2, h_4^2) in both the experiment and numerical simulation. Consequently, a snapshot of the potential field from the numerical simulation (Fig. 9) reflects the largest wave at $\omega_{lab}/\Omega_o = 1.5$. The strong Y_4^2 pattern in the numerical simulation is in excellent agreement with the experiment. Indeed the numerical simulations reproduce both the frequency and the principal spatial pattern of the two dominant waves in the experiments.

5. Large-eddy simulations

Numerical calculations at the exact conditions of the experiments require impractical improvements in spatial resolution to adequately represent the small-scale flow and magnetic field. Alternatively, we could attempt to resolve only the large-scale motions and model the influence of the small-scale flow and magnetic field. A large-eddy simulation relies on spatial filtering to eliminate the scales that cannot be resolved on the grid (Meneveau and Katz, 2000). Applying a spatial filter to the governing equations introduces additional terms to account for the influence of small-scale interactions between the flow and the magnetic field. One subgrid-scale term is required for each nonlinear term in the governing equations. A total of three subgrid-scale terms are needed for the problem of the spherical Couette flow in an electrically conducting fluid. The relevant terms include the Reynolds stress

$$\tau_{ij} = \overline{u_i u_j} - \overline{u}_i \overline{u}_j \tag{9}$$

the SGS Maxwell stress

$$M_{ij} = \Lambda(\overline{b_i b_j} - \overline{b}_i \overline{b}_j) \tag{10}$$

and the SGS induction term

$$a_i = \epsilon_{ijk}(\overline{u_j b_k} - \overline{u}_j \overline{b}_k) \tag{11}$$

where $\overline{u}_i$, $\overline{b}_i$, etc. denote the filtered fields implicit in representing **u** and **b** on a coarse grid; summation convention is assumed over repeated indices and ϵ_{ijk} is the alternating tensor. We model the SGS terms using the scale-similarity method of Germano (1986). For example, the model for the Reynolds stress is

$$\tau_{ij}^{sim} = C^{sim}(\widetilde{\overline{u}_i \overline{u}_j} - \widetilde{\overline{u}}_i \widetilde{\overline{u}}_j) \tag{12}$$

where $\widetilde{\overline{u}}_i$, etc. represent the effect of a second spatial filter on $\overline{u}_i$ that eliminates a larger fraction of the small scales (analogous to an even coarser grid) and C^{sim} is a model constant that adjusts the overall amplitude of the stress tensor. The other SGS terms are handled in a similar way. Matsui and Buffett (2007) developed a dynamic,

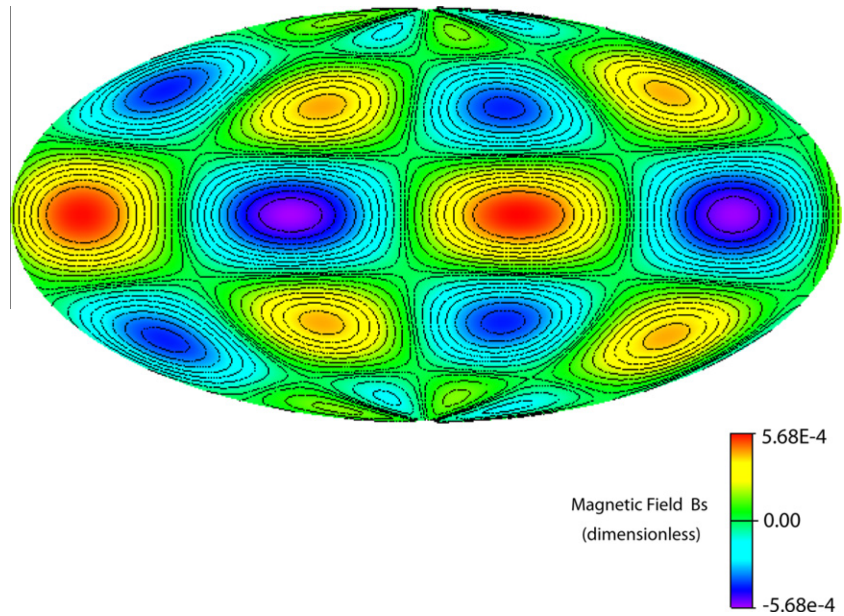

Fig. 9. Snapshot of the B_s component of the field from the numerical simulation. The field is evaluated at the position of the Hall probes ($r = 1.2r_o$). A strong Y_4^2 component in B_s is associated with the largest wave at $\omega_{lab}/\Omega_o = 1.5$. Comparison with the experimental results in Fig. 7 (left) reveals good agreement.

scale-similarity SGS model, which uses the large-scale fields, $\bar{\mathbf{u}}$ and $\bar{\mathbf{b}}$, to evaluate a model coefficient for each SGS term. This scheme was tested by Matsui and Buffett (2011) in simulations of a convection-driven dynamo in a rotating plane layer. Good agreement with the results of higher resolution calculations demonstrate the utility of the approach. In that particular application the model coefficients were averaged over a horizontal surface to reduce the spatial and temporal variability in the estimate of C^{sim}. In the present study we apply the same SGS model, but average the model coefficients over longitude. As a result, the model coefficients vary with radius and latitude.

We repeat the numerical calculations of the spherical Couette flow using a large eddy simulation on a grid with 1.5× coarser resolution in each dimension (roughly 3× fewer grid points). We retain the same fine radial resolution in the viscous boundary layers, eliminating the need for the SGS models in the boundary where the models often perform poorly. The initial condition is the same non-magnetic solution used in the direct numerical simulation, but interpolated onto the coarser grid. As before, the simulation is run for 2×10^5 time steps or about 12 s. Fig. 10 shows the time

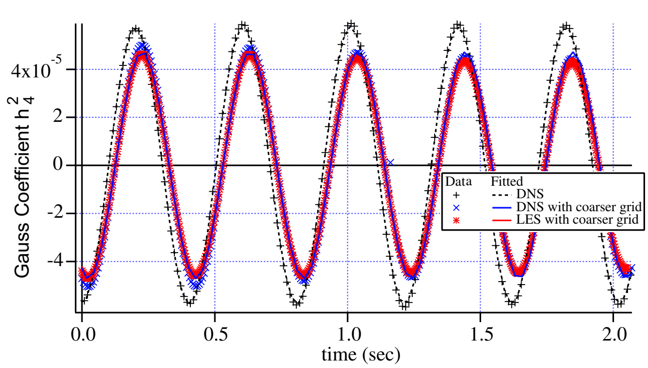

Fig. 10. Time dependence of Gauss coefficient h_4^2 from the large-eddy simulation (LES). The results are compared with the predictions of direct numerical simulations (DNS) on two different grids (coarse and fine). Individual points represent the result of the numerical calculations, whereas the solid line gives the best fitting sinusoid. The frequency of fluctuations in all three calculations are nearly identical, whereas the amplitude of the LES and DNS on the coarser grid have somewhat smaller amplitude.

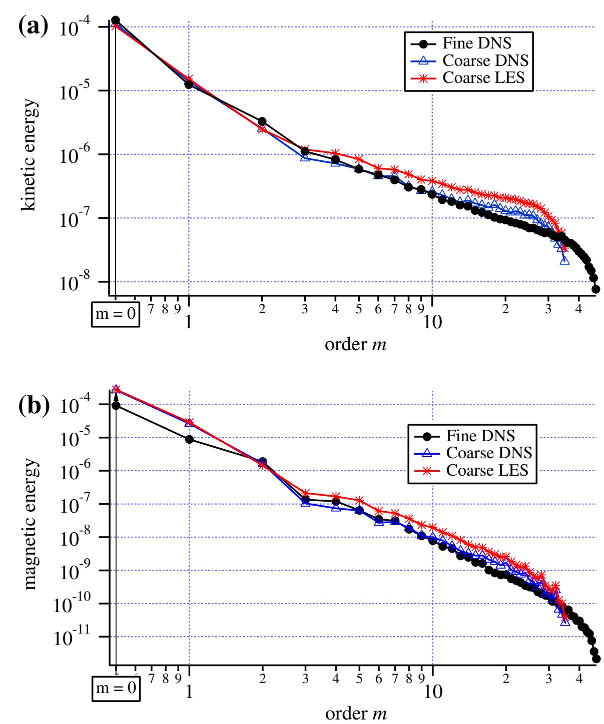

Fig. 11. Spatial spectrum of (a) kinetic energy and (b) magnetic energy as a function of angular order m for two solutions on the coarser grid (LES and DNS). Both coarse-grid solutions have higher energy at small scales compared with the resolved (fine) DNS.

evolution of the dominant Y_4^2 component of the external magnetic field (specifically the $h_4^2(t)$ Gauss coefficient) for the final 2 s of the run. We also obtain a direct numerical solution on the coarser grid with no SGS terms. Both of the numerical solutions on the coarser grid yield similar time variations in h_4^2. While the frequency of these variations is consistent with the resolved calculation, the amplitudes are somewhat smaller and may be still adjusting to a new equilibrium. Overall, the modest change in numerical resolution does not have a large effect on the structure of the mean flow or the dominant inertial waves that are excited by this flow.

A close agreement between the two solutions of the coarse grid (with and without the SGS terms) indicates that the SGS terms have only a small influence on the flow. The relative importance of these terms can be judged on the basis of their contribution to the global kinetic and magnetic energies. For example, the rate of work done by the Reynolds stress is about two orders of magnitude larger than that due to the SGS Maxwell stress. The Reynolds stress also exhibits large time variations. On average, the Reynolds stress transfers energy from the large-scale flow into the unresolved scales, but there are instances in which energy is transferred back into the large scales. These fluctuations have an unexpected effect on the large-scale flow. Fig. 11 shows time-averaged kinetic and magnetic energy spectra as a function of angular order m for both the coarse- and fine-grid results. The kinetic energies from all three calculations are in good agreement at the lowest angular orders ($m = 0$ and 1), but differences emerge at the smallest resolved scales. Both of the solutions on the coarse grid have more kinetic energy at high m than the resolved calculation. In fact, the kinetic energy in the LES is higher than that in the unresolved DNS, even though the time-averaged Reynolds stress transfers kinetic energy from the resolved scales into the unresolved scales. It appears that the fluctuations in the Reynolds stress inhibit the dissipation of kinetic energy at small scales, leading to a higher amplitude flow at these scales. The higher amplitude flow in the LES accounts for the larger magnetic spectra at small scales.

6. Discussion

Kelley et al. (2007) find close correspondence between the frequencies measured in the experiments and the frequencies of inertial oscillations in a sphere. Each inertial mode is specified by three indices (l,m,k), which reflect the spatial structure of the mode (e.g. Greenspan, 1968). The degree l and order m are symmetry numbers with the same meaning as in spherical harmonics, whereas k is loosely analogous to a radial wavenumber ($k = 1$ usually identifies the lowest frequency mode). Analytical expressions for the frequency and fluid velocity of each mode (e.g. Zhang et al., 2001) were used by Kelley et al. (2007) to match the magnetic perturbation outside the sphere. Modes that are antisymmetric about the equator ($l - m$ odd) produce symmetric magnetic perturbations ($l - m$ even), like those observed in the experiments. By matching the frequency and spatial structure of the observed magnetic perturbations, Kelley et al. (2007) identified peaks in the measured spectrum (Fig. 5) with specific inertial modes. Three modes are evident in both the experiments and simulations under the conditions considered in this study. A list of these inertial modes is given in Table 2, along with a comparison of frequencies from theory, simulations and experiments, all expressed in the laboratory frame.

Table 2
Identification of inertial modes based on spatial structure and frequency of waves in the laboratory frame. Indices (l,m,k) identify the mode and ω/Ω_o is the theoretical frequency in the rotating frame. Negative frequencies represent westward (retrograde) waves. A comparison of wave frequencies in the laboratory frame includes estimates from theory, the numerical simulation and the experiment.

Mode	ω/Ω_o	ω_{lab}/Ω_o		
		Theory	Simulation	Experiment
(4,3,1)	−0.500	2.500	2.543	2.485
(5,2,1)	−0.467	1.533	1.509	1.462
(6,1,1)	−0.440	0.560	0.627	0.568

Inertial oscillations in a fluid sphere give a good description of the frequency and spatial structure of the waves in the experiments. In some ways the agreement is surprisingly good because the theory neglects the influence of a solid inner sphere and the experiments generate waves in a fluid that is not uniformly rotating. Our numerical simulations show that the mean fluid motion outside the tangent cylinder is roughly in solid-body rotation with the outer solid shell. In this region the dynamics is well approximated by a rotating fluid (albeit a turbulent fluid). However, the fluid inside the tangent cylinder departs from uniform rotation with strong shear across Stewartson layers at the tangent cylinder.

The largest wave in both the experiments and simulations is associated with the (5,2,1) inertial mode. The structure of this particular mode is illustrated in Fig. 12 using the theoretical pressure field (Greenspan, 1968). A comparison of the pressure field from the direct numerical simulation (specifically at $m = 2$) reveals broad similarities (see Fig. 12). This agreement suggests that a large part of the pressure variation (and hence flow) at

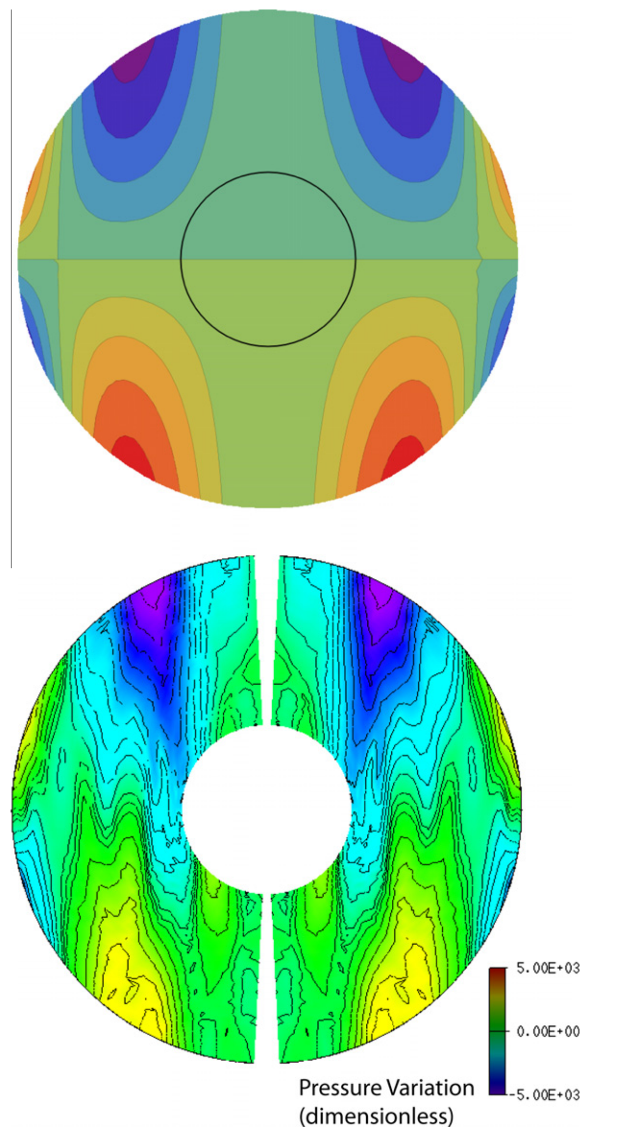

Fig. 12. A comparison of fluid pressure from theory and numerical simulation. (Top) A vertical cross section of the pressure perturbation due to the (5,2,1) inertial mode. (Bottom) A snapshot of pressure variations about the volume average from the numerical simulation. Only the $m = 2$ component of pressure is plotted to facilitate comparison with theory. A large part of the pressure variation from the numerical solution can be attributed to the (5,2,1) inertial mode.

Please cite this article in press as: Matsui, H., et al. Numerical and experimental investigation of shear-driven inertial oscillations in an Earth-like geometry. Phys. Earth Planet. In. (2011), doi:10.1016/j.pepi.2011.07.012

ARTICLE IN PRESS

$m = 2$ can be explained by the (5,2,1) mode. In both theory and simulation the pressure field is antisymmetric about the equator with relatively little variation inside the tangent cylinder. The numerical simulation indicates an abrupt change in pressure at the tangent cylinder, whereas the theoretical mode exhibits a more gradual decrease. However, the similarities in the pressure fields help to explain why the wave frequency in the simulation is well approximated by an inertial wave in a sphere.

Excitation of inertial waves appears to be weakly dependent on the structure of flow at small scales because the LES and the unresolved DNS yield similar results for the dominant waves, even though these solutions have different levels of kinetic energy at small scales. In both cases, flow is driven at the largest scale ($m = 0$) by differential motion of the boundaries; kinetic energy cascades to smaller scales through instabilities and nonlinearities in the governing equations. Details of this cascade appear to have little influence on the zonal flow ($m = 0$) or even the flow at $m = 1$. A very different situation is expected in convectively driven dynamo models because buoyancy drives flow across a broad range of scales. In this case a better estimate for the small-scale flow may be needed to make reliable predictions about the largest (observable) features of the flow or field.

Comparisons of the fine- and coarse-grid numerical results indicate that the scale-similarity model does not dissipate enough energy at the smallest scales. A similar conclusion was drawn by Winckelmanns et al. (2001), based on the simulations of homogeneous turbulence. Addition of an eddy viscosity to the SGS model (sometimes called a composite model) enhances dissipation and can give better results. The questionable performance of the scale-similarity model in the problem of the spherical Couette flow is not entirely surprising because the flow has some features in common with homogeneous turbulence. In particular, inertia has an important role in dynamics. Even though the spherical Couette flow exhibits aspects of rapid rotation (like the columnar structure at the tangent cylinder), the magnitude of the Rossby number is not much smaller than 1 (see Table 1). Consequently, inertia is a key nonlinearity in the governing equations. By comparison, the Rossby number in the Earth's core is nominally 10^{-6}, which makes inertia much less important. Small-scale turbulence in the core is more likely a result of small-scale buoyancy (Braginsky and Meytlis, 1990) than a result of inertial cascade. On the other hand, large-scale inertial waves are expected to be pervasive throughout the core (Aldridge and Lumb, 1987; Buffett, 2010).

7. Conclusions

The simulations and experiments reported here examine the excitation of inertial waves in flow driven by differential rotation of the boundaries. Despite the low Ekman number (and high Reynolds number) of the experimental flow, the simulations reproduce the dominant inertial modes observed in the experiments. Both the frequency and spatial structure of the modes are captured in the simulations. Moreover, the simulations reveal that the inertial modes are similar in structure to the theoretical predictions for a fluid sphere, although the modes appear to be distorted to fit within the region outside the tangential cylinder. Successful simulations required very fine radial grid spacing to resolve viscous boundaries. Less resolution was required in the interior of the fluid because the presence of a vertical magnetic field suppressed small-scale flow.

Benchmarking the numerical simulations with the results of the experiments is a first step in developing more sophisticated numerical models. Subgrid-scale models for the effects of unresolved flow and magnetic field variations are needed to achieve more demanding experimental conditions (notably faster rotation rates and weaker imposed magnetic fields). Because the small-scale flow is affected by rotation and magnetic field, we have an opportunity to test and refine subgrid-scale models. The scale-similarity SGS model is flexible enough to describe all SGS terms in the spherical Couette flow, although preliminary tests suggest that the Reynolds stress is most important for the range of conditions considered here. Fluctuations in the Reynolds stress had the unexpected effect of increasing the kinetic energy at small scales, even though the time-averaged rate of work by the Reynolds stress dissipated kinetic energy in the resolved scales. Supplementing the scale-similarity model with a dynamic eddy viscosity may be a simple remedy for dealing with strong turbulence.

References

Aldridge, K.D., Lumb, L.I., 1987. Inertial waves identified in the Earth's fluid outer core. Nature 325, 421–423.

Braginsky, S.I., Meytlis, V.P., 1990. Local turbulence in the Earth's core. Geophys. Astrophys. Fluid Dyn. 55, 71–87.

Buffett, B.A., 2010. Tidal dissipation and the strength of the Earth's internal magnetic field. Nature 468, 952–954.

Bullard, E., Gellman, H., 1954. Homogeneous dynamos and terrestrial magnetism. Phil. Trans. Roy. Soc. London A 247 (928), 213–278.

Chen, Q.N., Jones, C.A., 2008. Similarity and dynamic similarity models for large-eddy simulations of rotating convection-driven dynamo. Geophys. J. Int. 172, 103–114.

Germano, M., 1986. A proposal for a redefinition of the turbulent stresses in the filtered Navier–Stokes equations. Phys. Fluids 3, 2323–2324.

Greenspan, H.P., 1968. Theory of Rotating Fluids. Cambridge University Press, London, 328 pp.

Hollerbach, R., 2003. Instabilities of the Stewartson layer: Part 1. The dependence on the sign of Ro. J. Fluid Mech. 492, 289–302.

Kelley, D.H., Triana, S.A., Zimmerman, D.S., Tilgner, A., Lathrop, D.P., 2007. Inertial waves driven by differential rotation in a planetary geometry. Geophys. Astrophys. Fluid Dyn. 101, 469–487.

Kelley, D.H., Lathrop, D.P., 2010. Selection of inertial modes in spherical Couette flow. Phys. Rev. E 81, 026311.

Matsui, H., Okuda, H., 2005. MHD dynamo simulation using the GeoFEM platform—verification by the dynamo benchmark test. Int. J. Comput. Fluid Dyn. 19, 15–22.

Matsui, H., Buffett, B.A., 2005. A subgrid scale model for convection-driven dynamos in a rotating plane layer. Phys. Earth Planet. Inter. 153, 108–123.

Matsui, H., Buffett, B.A., 2007. A dynamic scale similarity model for dynamo simulations in a rotating plane layer. Geophys. Astrophys. Fluid Dyn. 101, 451–468.

Matsui, H., Buffett, B.A., 2011. Large-eddy simulations of a convection-driven dynamo using the scale-similarity method. Geophys. Astrophys. Fluid Dyn. doi:10.1080/03091929.2011.590806.

Matsushima, M., 2005. A scale-similarity model the subgrid-scale flux with application to MHD turbulence in the Earth's core. Phys. Earth. Planet. Inter. 153, 74–82.

Meneveau, C., Katz, J., 2000. Scale-invariance and turbulence models for large-eddy simulations. Annu. Rev. Fluid Mech. 32, 1–32.

Monchaux, R., Berhanu, M., Bourgoin, M., Moulin, M., Odier, P., Pinton, J.-F., Volk, R., Fauve, S., Mordant, N., Petrelis, F., Chiffaudel, A., Daviaud, F., Dubrulle, B., Gasquet, C., Marie, L., Ravelet, F., 2007. Generation of a magnetic field by dynamo action in a turbulent flow of liquid sodium. Phys. Rev. Lett. 98 (4), 044502–044504.

Press, W.H., Teukolsky, S.A., Vetterling, W.T., Flannery, B.P., 2007. Numerical Recipes: The Art of Scientific Computing, third ed. Cambridge University Press, London, 1256 pp.

Ribner, H.S., 1957. Reflection transmission and amplification of sound by a moving medium. J. Acoust. Soc. Am. 29, 435–441.

Rieutord, M., Valdettaro, L., 2010. Viscous dissipation by tidally forced inertial modes in a rotating spherical shell. J. Fluid Mech. 643 (1), 363–394.

Stewartson, K., 1966. On almost rigid rotations, Part 2. J. Fluid Mech. 26, 131–144.

Sisan, D.R., 2004. Hydromagnetic turbulent instability in liquid sodium experiments, Ph.D. Thesis, University of Maryland.

Sumita, I., Olson, P., 2003. Experiments on highly supercritical thermal convection in a rapidly rotating hemispherical shell. J. Fluid Mech. 492, 271–287.

Schmitt, D., Alboussière, T., Brito, D., Cardin, P., Gagnière, N., Jault, D., Nataf, H.C., 2008. Rotating spherical Couette flow in a dipolar magnetic field: experimental study of magneto-inertial waves. J. Fluid Mech. 604, 175–197.

Winckelmanns, G.S., Wray, A.A., Vasilyev, O.V., Jeanmart, H., 2001. Explicit filtering large-eddy simulation using the tensor-diffusivity model supplemented by a dynamic Smagorinsky term. Phys. Fluids 13, 1385–1403.

Zhang, K., Earnshaw, P., Liao, X., Busse, F.H., 2001. On inertial waves in a rotating fluid sphere. J. Fluid Mech. 437, 103–119.

Please cite this article in press as: Matsui, H., et al. Numerical and experimental investigation of shear-driven inertial oscillations in an Earth-like geometry. Phys. Earth Planet. In. (2011), doi:10.1016/j.pepi.2011.07.012